



## Bioresorbability Dependence on Microstructure of Additively-Manufactured and Conventionally-Produced Fe-Mn Alloys

Matjaž Godec<sup>a,\*</sup>, Jakob Kraner<sup>a,b</sup>, Danijela Skobir Balantič<sup>a</sup>, Irena Paulin<sup>a</sup>, Damjana Drobne<sup>c</sup>, Veno Kononenko<sup>c</sup>, Aleksandra Kocijan<sup>a</sup>, Paul McGuinness<sup>a</sup>, Črtomir Donik<sup>a</sup>

<sup>a</sup> Institute of Metals and Technology, Ljubljana, Slovenia

<sup>b</sup> Impol 2000 d.d., Slovenska Bistrica, Slovenia

<sup>c</sup> Biotechnical Faculty, University of Ljubljana, Slovenia

### ARTICLE INFO

Handling editor: P.Y. Chen

#### Keywords:

Fe-Mn alloy  
laser powder bed fusion  
bioresorbable  
microstructure  
corrosion behaviour  
biocompatibility

### ABSTRACT

Fe-Mn alloys were produced for bioresorbable applications using the laser powder bed fusion (LPBF) process with varying process parameters. The feedstock alloy powder for LPBF was derived from conventional cast/forged bars using plasma ultrasonic atomization. Additionally, a conventionally produced Fe-Mn alloy with the same composition was investigated to compare material properties. The influence of the processing route and LPBF process parameters on microstructure evolution, particularly the formation of  $\Sigma$  boundaries, was examined and correlated with the observed corrosion rate obtained from potentiodynamic curves in Hank's solution. The concentration of released Fe and Mn ions after immersion tests in lactic acid was also evaluated. The initial corrosion mechanism of the LPBF alloy was elucidated through X-ray photoelectron spectroscopy (XPS). Furthermore, *in vitro* tests were conducted using MG-63 human osteoblast-like osteosarcoma cells to assess the biocompatibility response. The present study established a correlation between microstructure and corrosion rate, while the biocompatibility tests affirmed the suitability of additively manufactured Fe-Mn alloys for bioresorbable applications.

### 1. Introduction

Bioresorbable metals and their alloys represent a step forward in medical implant applications due to their ability to degrade inside the body. As such, they can serve as temporary cardiovascular, orthopaedic or bone substitutes with no need for revision surgery and removing the permanent implants [1,2]. Magnesium, zinc, iron and molybdenum, as well as their alloys, are among the most studied bioresorbable metallic materials. All of them have some advantages (Mg-based alloys have healing effect and similar mechanical properties to bone, Fe-based alloys have extreme mechanical properties) and disadvantages (degradation of Mg-based alloys causes excess of gas, Fe-based alloys degrade too slowly); therefore, they are used for various medical application studies [3].

The research of Fe-based alloys as bioresorbable materials has made considerable progress in recent years. However, preparing material with all the desirable requirements regarding mechanical properties, non-magnetic microstructure (suitable for magnetic resonance imaging

(MRI)), biocompatibility, degradation rate, and production suitability is still challenging. The main disadvantage of Fe-based bioresorbable alloys still remains their slow degradation, which is the focus of numerous research studies [2,4,5]. In order to achieve non-magnetic phase ( $\gamma$ -austenite) enabling MRI compatibility, it is crucial to establish the appropriate Mn-C ratio. Manganese demonstrates weak passivity characteristics and forms an unstable MnO film, leading to increased corrosion current ( $i_{corr}$ ) and reduced corrosion potential ( $E_{corr}$ ) values [6]. When added as an alloying element, carbon can stabilise austenite and strengthen the matrix through solid solution strengthening. Specifically, for alloys containing less than 25 wt.% manganese to maintain stable austenite at room temperature, the creation of  $\epsilon'$ - and  $\alpha'$ -martensite needs to be suppressed. Introducing approximately 0.6 wt.% of carbon facilitates the development of carbide-free austenitic structures, effectively preventing the formation of  $\alpha$ -martensite. Nonetheless, incorporating carbon in higher quantities leads to the formation of carbides ( $M_3C$ ) [7]. Hermawan et al. [8–10] reported on the various Fe-Mn alloys with 20–35 wt.% Mn with suitable corrosion and

\* Corresponding author, Institute of Metals and Technology, Lepi pot 11, 1000 Ljubljana, Slovenia

E-mail address: [matjaz.godec@imt.si](mailto:matjaz.godec@imt.si) (M. Godec).

<https://doi.org/10.1016/j.jmrt.2024.04.097>

Received 12 February 2024; Received in revised form 8 April 2024; Accepted 11 April 2024

Available online 16 April 2024

2238-7854/© 2024 Published by Elsevier B.V. This is an open access article under the CC BY-NC-ND license (<http://creativecommons.org/licenses/by-nc-nd/4.0/>).

non-magnetic behaviour. Lee et al. [11] reported that the nonmagnetic  $\gamma$  phase is reached around 28 wt.% Mn and C content above 0.02 wt.%. The use of nonmagnetic carbonless Fe-Mn alloy requires a larger percentage of Mn. However, this creates challenges for the LPBF process because the high amount of Mn results in increased evaporation [12]. The studies in the literature are therefore mostly focused on alloying with Mn and C [4,13–17] as well as the addition of other alloying elements: Pd, Ag, S, Cu and B to promote the corrosion rate [5,18,19], Ca and Mg for enhanced biocompatibility and lower cytotoxicity [20]. Mandal et al. [19] reported that adding Cu also acts as an antimicrobial agent, stabilises austenite, and causes better osteogenesis and new bone formation. The addition of Ag increases the corrosion rate [21,22] and antimicrobial properties of the alloy, although its antimicrobial role remains controversial. Some studies confirmed antibacterial activity [21] and improved resistance to infections [23], while Liu et al. [24] observed no effect on antimicrobial properties with the addition of Ag. Fe-Mn alloys are further known for their relatively good degradation *in vitro*, while *in vivo*, they show a low degradation rate due to differences in testing conditions and actual implant environment [25].

Another important issue addressing the material's degradation behaviour is the processing route. The majority of studies have been performed on conventionally produced Fe-Mn alloys [18,19,23,26,27], and only recently have some studies been performed on LPBF-processed alloys [12,28–32]. LPBF enables the fabrication of patient-specific implants as well as structures with large surface-to-bulk and porous structures, which increase the degradation rate [28–31]. The LPBF-processed Fe-Mn alloys can be produced from pure elemental powders [12,30] prepared by mechanical mixing and alloy powders [28–33]. Using pure elemental powders causes high evaporation of Mn and the difficulties of obtaining a homogeneous structure with only  $\gamma$ -austenite phase [12,30]. Studies of the corrosion rate have shown that with an increased amount of Mn, the corrosion rate increases due to a change in the oxide layer behaviour [34]. Carluccio et al. [29] studied corrosion products on LPBF Fe-Mn scaffold and reported different products depending on the scaffold position. They found areas rich in P and Ca and also areas with higher Fe-oxide and Mn-oxide concentrations. Gambaro et al. [26] investigated corrosion products by XPS and reported the formation of a barrier layer ((Fe,Mn)CO<sub>3</sub>) for corrosion.

Results of biocompatibility tests on LPBF Fe-Mn material using MC3T3-E1 mouse preosteoblast cells [29,31,35] and human vascular muscle cells [28] have also been reported, with promising results. The biocompatibility of new biomaterials in the material research phase is first tested *in vitro* with different cell lines, as implantable biomaterials should be non-cytotoxic and should allow good cell adhesion, which is crucial for the proliferation and spreading of cells on the surface of the implant [36]. Biomaterials being developed for various biomedical applications can be tested with respect to osteoblast adhesion and viability [37,38].

Although the literature studies include many Fe-Mn-C systems with different element additions, the compositions of around 30 wt.% Mn and 1 wt.% C are among the most studied [28,39,40] due to their LPBF suitability and ability to obtain the desired properties. Therefore, the present work is focused on the basic Fe-Mn-C to provide a comprehensive understanding of biodegradation differences between LPBF-processed Fe-Mn alloys and conventionally manufactured ones. The influence of the LPBF process parameters (laser power and laser scan speed) on the microstructure formation was investigated. Furthermore, the correlation of the microstructural features, particularly  $\Sigma$  grain boundaries, on the corrosion rate of LPBF- and conventionally-processed alloys was examined. Based on the XPS analyses, the initial corrosion mechanism observed after short-term exposure was proposed. Based on the corrosion results, the main detrimental impact on the degradation was suggested. The material is developing for orthopaedic implants and maxillofacial applications for bone reconstruction. Therefore, the investigation was supported by *in vitro* biocompatibility tests and cell analysis, using Hank's solution and lactic

acid and MG-63 cells.

## 2. Materials and Methods

### 2.1. Materials preparation

The investigated samples were prepared from two LPBF-processed Fe-Mn alloys. The feedstock alloy powder for LPBF was self-produced from conventional (cast/forged) bars. Samples from conventional (cast/forged) material were investigated as well and used as a comparable (control) material.

A conventional, custom-made Fe-Mn alloy was created by adding Mn and C to pure Fe, melting it in an induction furnace under an air atmosphere at around 1700 °C, and then gravity die-cast into 60 mm × 60 mm × 300 mm ingots. The ingots were hot forged from 1100 °C into 25 mm and 10 mm diameter bars. After forging, bars were annealed at 1050 °C for 20 min and quenched in water.

The Fe-Mn pre-alloy for powder preparation was prepared in the same way as final bars with a diameter of 10 mm as input material for atomisation. The powder for the LPBF process was prepared by plasma ultrasonic atomization with the rePowder (AMAZEMET, Poland) machine. The size of the gas-atomized powders used in this study was measured by a laser diffraction particle size analyser (Beckman Coulter LSTM 13 320). The average particle diameter for the Fe-Mn powders was 53.5  $\mu$ m, with D10, D50 and D90 values of 17.5  $\mu$ m, 49.2  $\mu$ m and 95.1  $\mu$ m, respectively. The average particle size for the Fe-Mn was 52.8  $\mu$ m, with D10, D50 and D90 values of 14.5  $\mu$ m, 48.0  $\mu$ m and 94.7  $\mu$ m, respectively.

Due to high Mn evaporation, the chemical composition of cast and forged bars was tailored with higher Mn content to reach the final composition of LPBF alloy around 33 wt.% Mn. The Mn concentration in the conventionally produced control samples was targeted to the same value.

An AconityMINI (Aconity3D, Germany) LPBF system, with the single mode infrared fibre laser (400 W), was employed to produce two different types of cylindrical samples with a dimension of  $\phi$  15 mm and height 20 mm. Laser power of 200 W and 350 W with a scan speed of 400 mm/s and 700 mm/s were used to manufacture two LPBF Fe-Mn alloys (LPBF 200/400 and LPBF 350/700). The process parameters were selected so that absorbed energy was exactly the same for both sets of samples. Samples slice thickness of 30  $\mu$ m and hatch spacing of 80  $\mu$ m were performed. A stripe pattern with a width of 10 mm and a shift between layers was applied, and the rotation between adjacent layers was 33°.

The chemical compositions of Fe-Mn cast and forged bars, as well as powders and LPBF processed samples, were measured by the Optical emission spectrometer with inductively coupled plasma (ICP-OES) with the Agilent 720 (Agilent Technologies, USA) and are presented in Table 1.

### 2.2. Microstructural Characterisation

A range of standardized analytical techniques were employed to gain a clear and detailed understanding of the microstructure of metallographic samples. These included mounting the samples in conductive Bakelite resin and carefully grinding and polishing them.

**Table 1**  
Content of C and Mn in wt.% (Fe balance).

Material	C	Mn
cast/forged bars for powder production	1.22 ± 0.05	36.2 ± 0.3
powder	1.19 ± 0.05	33.6 ± 0.3
LPBF alloy (200/400)	1.20 ± 0.05	32.8 ± 0.3
LPBF alloy (350/700)	1.21 ± 0.05	32.7 ± 0.3
control cast/forged bars	1.18 ± 0.05	32.5 ± 0.3

For even greater precision and detailed analyses, a Zeiss CrossBeam 550 FIBSEM field-emission scanning electron microscope (Carl Zeiss, Jena, Germany), equipped with an EDAX Hikari Super electron-backscatter diffraction (EBSD) camera and EDAX Octane Elite energy-dispersive spectroscopy (EDS) detector with APEX software, was used. This allowed for various analyses, including secondary-electron imaging, EDS and EBSD. In order to achieve the most suitable results, a range of parameters were employed, including a 15-kV accelerating voltage and 2.0–5.0 nA probe current for SE images and EDS analyses. For EBSD analyses, we utilized 70°-tilted samples and a 7.0-nA probe current.

To determine the phase composition, a Panalytical X'PERT Pro PW 3040/60 goniometer (Netherlands) with Bragg-Brentano geometry was used to perform X-ray Diffraction (XRD). To achieve the best possible results, a Cu anode with ( $K_{\alpha} = 0.154$  nm) at 40 mA and 45 kV, with a scan step time of 100 s at each step, and a  $2\theta$  goniometer ranging from 15° to 90° with a step size of 0.002° was used.

Finally, the Versa Probe 3 AD (Phi, USA) with a monochromatic Al  $K_{\alpha}$  X-ray source was used to perform photoelectron spectroscopy (XPS). A charge neutralizer and acquired spectra on a 200  $\mu\text{m}$  analysis spot size for thick, uncondusive oxides on the surface after immersion were used. Survey spectra were measured at a pass energy of 224 eV and a step of 0.5 eV and high-resolution (HR) XPS spectra at a pass energy of 69 eV and a step of 0.1 eV using vacuum  $3.5 \times 10^{-7}$  mbar. Three cycles for survey spectra and at least 15 cycles for all HR spectra measurements were performed. The carbon C 1s peak with the binding energy (BE) of 284.7 eV was used to correct possible charging effects. The acquired spectra were processed with MultiPak 9.9.2 ULVAC-PHI software with Shirley background subtraction. The BE scale accuracy was estimated to be 0.2 eV. High-resolution spectra for C 1s, O 1s, Mn 2p<sub>3/2</sub> and Fe 2p<sub>3/2</sub> were analysed. An Ar<sup>+</sup> ion sputtering was used to remove the sample's top layer. This involved sputtering the sample with 500 V over a  $1 \times 1$  mm area in the middle of the sample with a measured sputtering rate of approximately 2.6 nm/min of SiO<sub>2</sub> on the Si wafer. To ensure even sputtering and prevent ripening, a Zalar rotation was carried out. Immediately after sputtering, the HR spectra for C 1s, O 1s, Mn 2p and Fe 2p on a spot area in the middle of the sample were obtained.

### 2.3. Electrochemical and static immersion testing

The additively manufactured samples were evaluated in terms of corrosion by using potentiodynamic measurements and static immersion tests. All the samples were mechanically prepared with SiC paper up to 4000 grit and polished to a mirror finish. Before the measurements, the samples were washed with acetone and deionised water and finished by air drying. Potentiodynamic curves were recorded in standard Hank's solution (8 g/L NaCl, 0.40 g/L KCl, 0.35 g/L NaHCO<sub>3</sub>, 0.25 g/L NaH<sub>2</sub>PO<sub>4</sub> × 2H<sub>2</sub>O, 0.06 g/L Na<sub>2</sub>HPO<sub>4</sub> × 2H<sub>2</sub>O, 0.19 g/L CaCl<sub>2</sub> × 2H<sub>2</sub>O, 0.41 g/L MgCl<sub>2</sub> × 6H<sub>2</sub>O, 0.06 g/L MgSO<sub>4</sub> × 7H<sub>2</sub>O, 1 g/L glucose, pH = 7.8, Sigma-Aldrich chemicals) by using Potentiostat/Galvanostat BioLogic SP 300 (France) with EC-Lab V11.27 software. A three-electrode system was used with the examined sample as a working electrode (exposed area of 1 cm<sup>2</sup>), a saturated calomel electrode (SCE, 0.242 V vs. SHE) as a reference electrode and a Pt mesh as a counter electrode. Potentiodynamic measurements were performed at the scan rate of 1 mV/s by sweeping the potential from -250 mV vs. OCP until the current density reached 1 mA/cm<sup>2</sup>. The samples were stabilised at the open-circuit potential for 1 h prior to the experiment, the measurements were repeated three times to obtain statistically relevant results, and a scan rate of 1 mV/s was applied. Static immersion tests were performed by mounting the specimens in the 0.1 M lactic acid at 37 °C for 7 days according to ISO standard ISO 10271:2020 [41] (cross-referenced in ISO 22674:2022 [42]). The use of Hank's solution for corrosion tests is common for corrosion study of biocompatible metallic materials, while lactic acid is used in standardised immersion test. The bone implants *in vivo* are in contact with both media (Hank's solution is simulated physiological solution, lactic acid is present in muscles). The samples

were gravimetrically assessed by Radwag AS 220.3Y analytical balance before and after the immersion test. The concentration of dissolved species was measured after immersion using inductively coupled plasma optical emission spectroscopy (ICP-OES, Agilent 5800 VDV).

### 2.4. Biocompatibility testing

The biocompatibility of different Fe-Mn samples was evaluated *in vitro* using MG-63 human bone osteosarcoma cells (ATCC® CRL-1427™) grown on the sample surface. Use of bone osteosarcoma cells is suitable for orthopaedical and maxillofacial implants study due to get information of osteointegration of bone tissue during metal degradation. The surface finishing of all three studied samples was polished with 1 $\mu$  diamond suspension. Differential staining and fluorescence microscopy were used to evaluate the adhesion and viability of MG-63 cells. The morphology of the cells adhered to the samples was examined using a scanning electron microscope (SEM). Prior to the experiments, the MycoAlert™ kit (Lonza, Basel, Switzerland) was used to confirm that the cells were mycoplasma negative. Cells were cultured under controlled conditions (37 °C, 5 % CO<sub>2</sub>, 95 % humidity) in Dulbecco's modified Eagle's medium (DMEM) supplemented with 4 mM L-glutamine, 10 % (v/v) fetal bovine serum (FBS), and 1 % Penicillin-Streptomycin solution (Sigma-Aldrich, Steinheim, Germany). Fe-Mn samples were UV-C sterilised for 30 minutes and aseptically placed in 12-well plates. Glass coverslips (Paul Marienfeld, Germany) were used as a control group. MG-63 cells ( $2 \times 10^4$  cells/cm<sup>2</sup>) were seeded into each well and incubated for 24 hours. After incubation, samples with adhered cells were rinsed in Dulbecco's Phosphate-Buffered Saline and stained with 2  $\mu\text{g}/\text{mL}$  Hoechst 33342 (Sigma-Aldrich, Steinheim, Germany) and 2  $\mu\text{g}/\text{mL}$  Propidium iodide (Sigma-Aldrich, Steinheim, Germany) for 20 min. The stained cells were observed with a fluorescence microscope (Axio Imager.Z1; Carl Zeiss, Jena, Germany). At least 10 images per sample were taken randomly at 100 $\times$  magnification, and each sample was examined in triplicate. The density and viability of attached cells were quantitatively analysed using ImageJ software. All results were normalised to the sample surface area. The cell adhesion assay data were expressed as arithmetic mean  $\pm$  standard deviations (SD) and statistically analysed using GraphPad Prism software (GraphPad Software, San Diego, CA) by the ANOVA with multiple comparison post hoc tests. The p-values less than 0.05 were considered statistically significant.

After fluorescence microscopy, the samples with attached cells were further prepared for SEM examination, as described in Hočevar et al. [38]. Briefly, samples with attached cells were fixated with 2.5 % glutaraldehyde and 0.4 % paraformaldehyde in 1 M Na-phosphate buffer. After 3 h fixation, the samples were post-fixed by 1 % Os-tetroxide and dehydrated with ethanol and hexamethyldisiloxane (HMDS). Dry samples were sputter coated with Au/Pd thin film in Gatan PECS system. Zeiss CrossBeam 550 FIB-SEM field-emission scanning electron microscope was used to visualize the attachment pattern and morphology of adhered MG-63 cells on glass coverslips and different Fe-Mn samples.

## 3. Results

### 3.1. Materials Characterisation

The plasma-ultrasound method was utilized to produce the feedstock powder for the LPBF process. This resulted in the production of practically ideal spherical powder particles that were used for the process, with a size range of 40–70  $\mu\text{m}$  (as shown in Fig. 1(a)). However, obtaining the desired chemical composition of the final powder particles was challenging due to the low vapour pressure of Mn, which caused its evaporation during the atomisation. The SEM/EDS analysis of a large number of particles showed a high variation in the amount of Mn and Fe present, which did not depend on the particles' size or area of analyses. The amount of Mn in the powder particles varied between 14 and 40 wt.

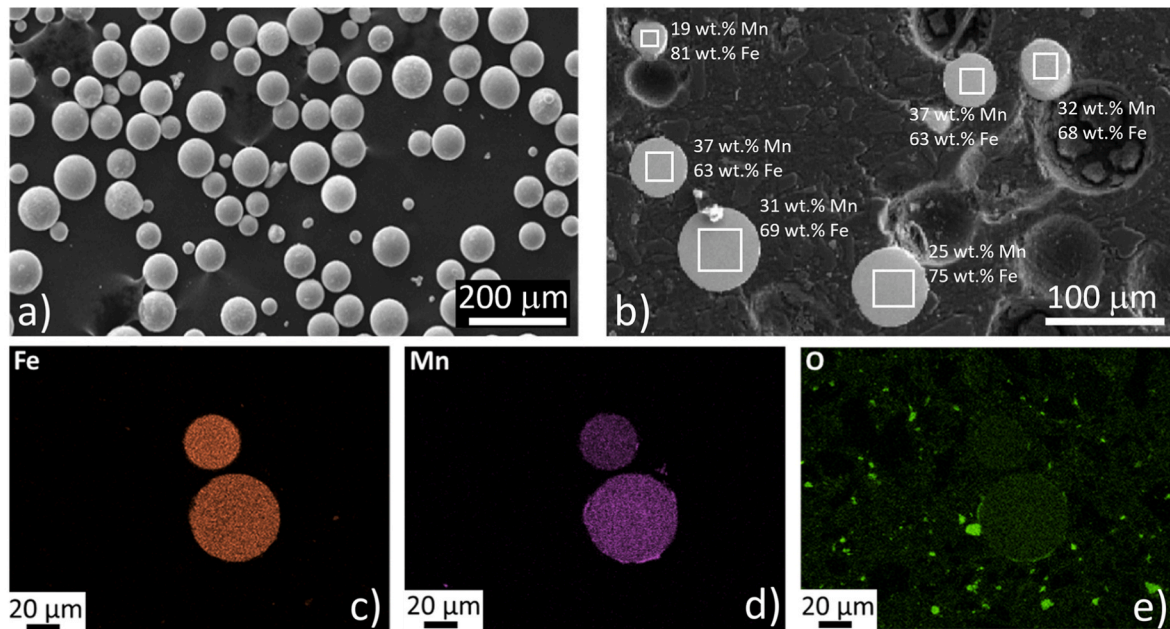


**Fig. 1.** The Fe-Mn powder manufactured by the plasma-ultrasound method: (a) SEM/SE image of powders on graphite tape, (b) cross-section of powders with EDS chemical analysis, (c–e) elemental distribution of Fe, Mn and O, respectively.

% (as presented in Fig. 1(b)). The distribution of Fe, Mn, and O in the powder particles was observed through SEM/EDS analysis, and it was found that Fe and Mn were quite equally distributed in the cross-sections of the particles. Additionally, a majority of the particles had a thin Mn oxide noncontinuous layer (as seen in Fig. 1(c)–(e)).

For both permanent and bioresorbable implants, the metallic materials utilized must be completely compatible with medical diagnostics such as magnetic resonance imaging (MRI). It is, therefore, absolutely crucial that these materials are nonmagnetic. Lee et al. [11] reported that the nonmagnetic  $\gamma$  phase is reached around 28 wt.% Mn and C content above 0.02 wt.%. The use of nonmagnetic carbonless Fe-Mn alloy requires a larger percentage of Mn. However, this creates challenges for the LPBF process because the high amount of Mn results in increased evaporation [12].

We utilized carbon-containing alloy powder in the LPBF process to produce samples. The resulting microstructure was austenitic and consisted of a single nonmagnetic phase ( $\gamma$ -phase) with a uniform Mn distribution, as shown in the inset of Fig. 2 (EDS Mn distribution). At the nano level, it has been observed that Mn segregates along cellular boundaries [43]. Based on a multicomponent phase field method coupled with thermodynamic calculations [44] and experiments [45] it was shown that Mn and C segregate at the same positions. However, due to the high concentration of C (1.2 wt. %) the Mn and C depletion does not reach a level where the ferrite or  $\varepsilon$ -martensite phase is formed. Fig. 2 shows the XRD spectra of Fe-Mn alloys produced by different processing routes. XRD spectrum of Fe-Mn alloy produced by LPBF using alloy-powder (spectrum A) shows only peaks of  $\gamma_{\text{FeMn}}$ . The XRD spectrum from the previous investigation [28] of Fe-Mn alloy produced by LPBF using pure elemental powders (spectrum B) is shown as a comparison. It is evident that the use of pure elemental powders leads to the formation of  $\gamma_{\text{FeMn}}$  and  $\varepsilon_{\text{FeMn}}$  phases and a small amount of MnO. MnO is formed from the trace amount of oxygen found in manganese powder particles. The spectrum of the cast and forged samples (spectrum C) of the material with the same chemical composition is similar to the spectrum of Fe-Mn alloy produced by LPBF using alloy powder (spectrum A). One of the noticeable differences is also the orientational effects, which result from grain texturing during the conventional cooling of the cast-and-forge process. This difference is reflected in the relative heights of the main two peaks. During conventional production

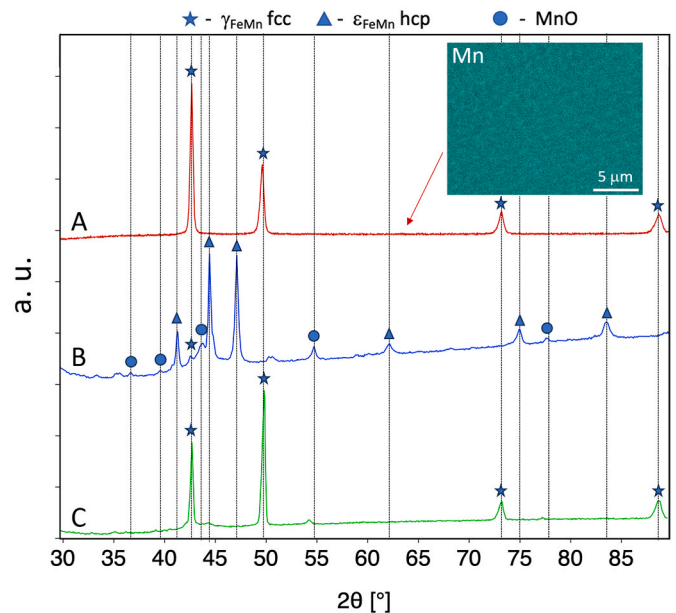


**Fig. 2.** XRD spectra of differently processed Fe-Mn alloys: (a) LPBF processed from alloy powders, (b) LPBF processed from pure elemental powders, and (c) cast and forged alloy. The inset represents the EDS elemental distribution of Mn.

processes like casting and forging, even in the austenite phase, there may be some small amount of MnO due to manganese's high affinity for oxygen. In the literature, several studies [2,46,47] were also performed on Fe-based alloys with lower Mn content, resulting in martensite magnetic phases. The presence of a multiphase structure may result in a higher corrosion rate and better mechanical properties [10]. However, such an alloy is less proper for applications in human bodies.

In Fig. 3, the microstructure of additive and conventionally manufactured Fe-Mn alloys is shown. The AM samples have columnar grain shapes and areas with similar grain orientations formed from nano to micro dendrites (Fig. 3(a) and (c)), while conventionally produced Fe-

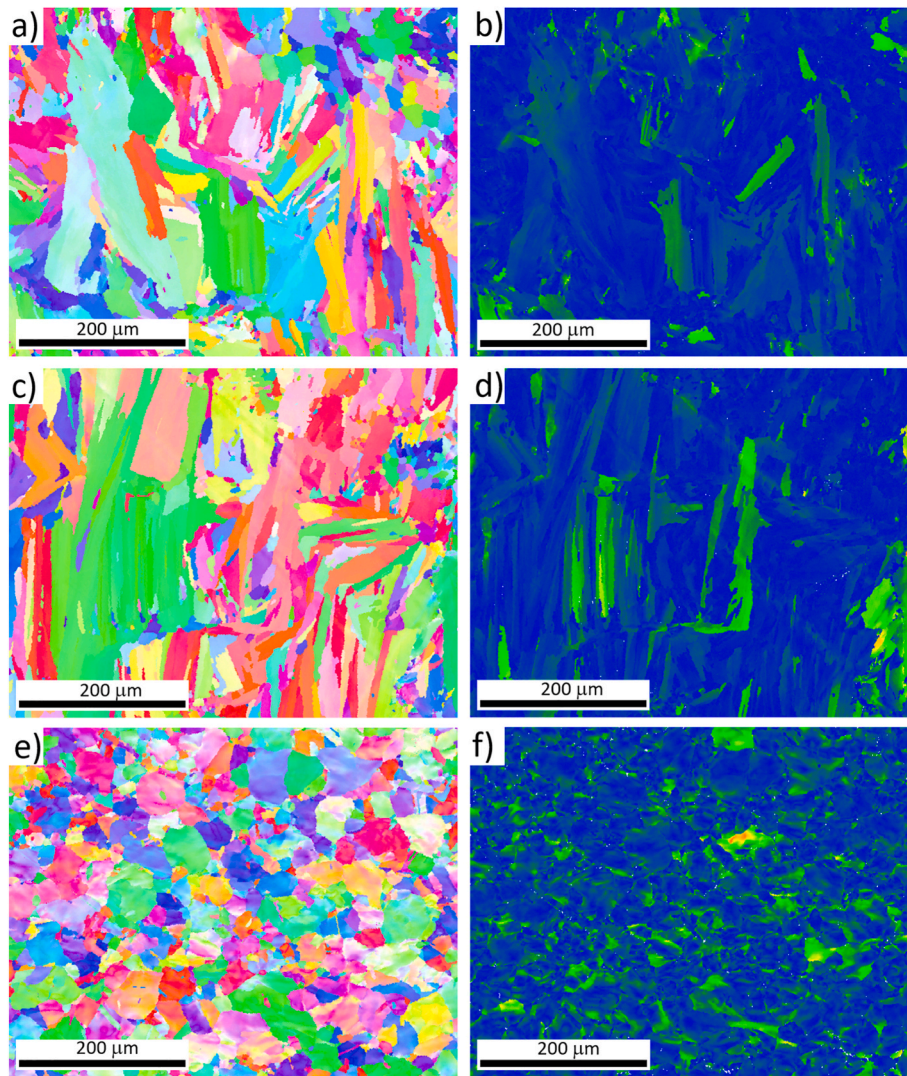


**Fig. 3.** Microstructures of Fe-Mn alloys prepared in different ways with the corresponding GROD images: (a) EBSD IPF-Z of LPBF processed Fe-Mn using 200/400 parameters, (b) GROD image, (c) EBSD IPF-Z of LPBF processed Fe-Mn using 350/700 parameters, (d) GROD image, (e) EBSD IPF-Z of the cast and forged Fe-Mn, (f) GROD image.

Mn exhibit equiaxed crystal grains (Fig. 3(e)). Two different LPBF processing parameters were used, which manifest with different GROD (Grain Reference Orientation Deviation) maps. Both selected parameters were chosen in such a way that the input energy was exactly the same. The average orientation for the grain was also calculated. Each point in a grain is shaded according to the misorientation, which reflects how a given point in a grain is bent or rotated in reference to the mean orientation of the entire grain. The GROD analysis shows different misorientation intensities of two LPBF samples and conventionally produced samples. The sample produced with higher laser power and higher laser scan speed (350/700) has twice higher GROD intensity than those produced with lower laser power and lower scan speed (200/400). On the other hand, the GROD intensity of conventionally produced samples is similar to sample LPBF 200/400. It has been observed that in a conventionally produced sample (Fig. 3(e) IPF-Z EBSD), the recrystallisation took place during the normalisation process, but it was not completed, indicated by misorientation within each grain.

To assess the electrochemical stability and degradation behaviour of Fe-Mn processed using LPBF potentiodynamic measurements and short-term static immersion tests were performed. The potentiodynamic behaviour of the investigated samples in Hank's solution with the corresponding corrosion rates ( $v_{\text{corr}}$ ), as well as the concentration of the

released Fe and Mn ions after the short-term immersion tests in 0.1 M lactic acid, are presented in Fig. 4. The calculations of the  $v_{\text{corr}}$  were made according to ASTM G102 – 89 (2015) [48]. The results showed that the conventionally produced Fe-Mn alloy had the highest corrosion potential as well as the lowest corrosion rate in contrast to the Fe-Mn samples produced through LPBF production route. LPBF processed samples displayed lower corrosion potentials and several times higher corrosion rates, despite the use of an equal input energy. The sample processed at 350/700 laser power and speed exhibited significantly lower corrosion resistance. This is in correlation to the results obtained in short-term immersion tests, where the concentrations of the released Fe- and Mn- species in lactic acid were higher for LPBF samples, especially for 350/700 (Fig. 4b).

Potentiodynamic polarization measurements enable us to understand the reactions, rate determining processes, and the stability of the passive film under the controlled laboratory conditions. They may differ significantly from long-term exposures in real-life conditions; however, they allow us to estimate and to compare the corrosion behaviour of the samples exposed to different parameters and conditions. The corrosion rates determined by using the Tafel extrapolation method are accurate if at least one part of the polarization curve is under activation control, the corrosion is uniform, a Tafel region is well-defined and electrode-

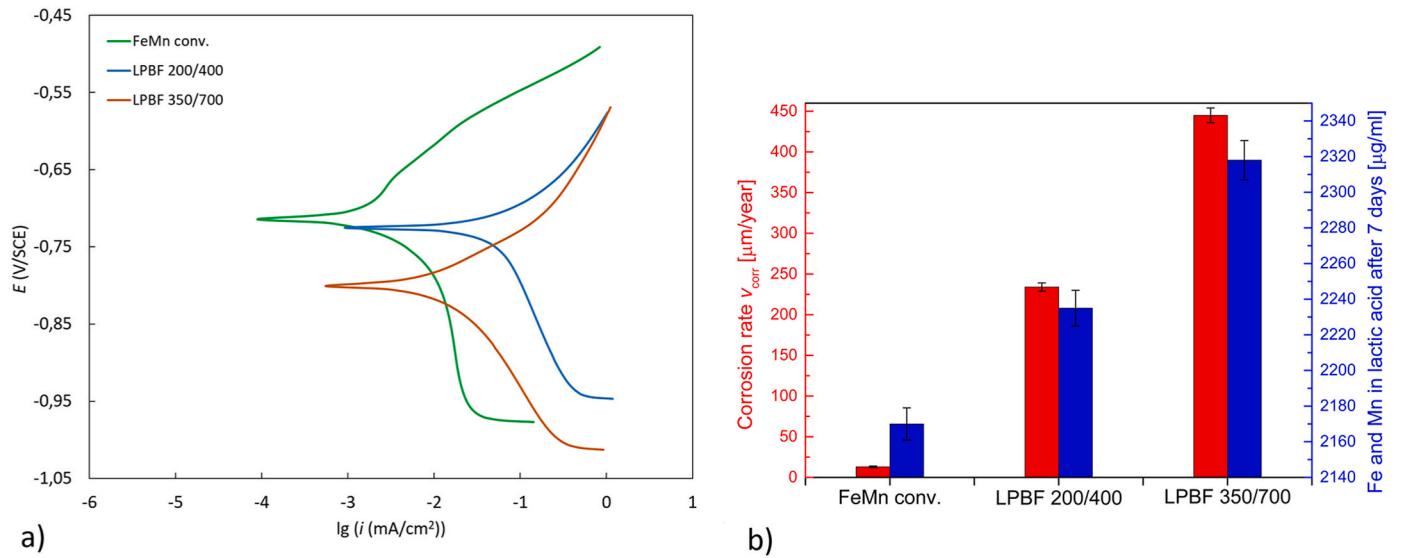


Fig. 4. (a) Potentiodynamic curves, (b) corrosion rate and Fe-Mn behaviour in lactic acid dependent on production route.

potential changes do not affect additional electrode reactions [49].

The intergranular corrosion properties are related to coincidence lattice site (CLS) grain boundaries. Better corrosion resistance is obtained by a higher proportion of the sum of CLS boundaries vs. all boundaries, and typically, lower sigma values, like  $\Sigma 3$ , are more effective in resisting corrosion compared to higher sigma values, such as  $\Sigma 27$  [50,51]. After a week of exposure to Hank's solution, the Fe-Mn alloy shows corrosion along grain boundaries, while the CLS boundaries remain mostly unattacked (Fig. 5). The pitting corrosion is also observed inside the grains but is much less intensive compared to that on regular grain boundaries.

In order to adequately evaluate the corrosion rates of the investigated samples, it is necessary to identify any correlations with specific  $\Sigma$  grain boundaries. The corrosion properties of materials can be influenced in various ways by the sigma values of grain boundaries, such as  $\Sigma 3$ ,  $\Sigma 9$ , and  $\Sigma 27$  [50]. Nevertheless, the correlation between these sigma values and corrosion properties is not simple and can depend on multiple factors. Therefore, the higher degree of coincidence between adjacent grains in lower sigma boundaries provides a better barrier to the movement of corrosive species. On the contrary, higher sigma boundaries are less stable and have more structural defects, which makes them more susceptible to corrosion attack. The impact of sigma values on corrosion properties can vary based on the material's environment. It is known from the literature data [50] that higher sigma boundaries can be less vulnerable to stress corrosion cracking due to their intricate structure and lower dislocation mobility. On the other

hand, lower sigma boundaries may be more prone to pitting corrosion because of their instability and the presence of grain boundary sites susceptible to corrosion.

Austenitic Fe-Mn-Al-Cr-C twinning-induced plasticity alloy that has undergone conventional processing is known for its high corrosion resistance due to its numerous  $\Sigma 3$  boundaries [51]. However, materials processed via LPBF exhibit fewer  $\Sigma 3$  boundaries, potentially leading to inferior corrosion properties and reduced resistance. A comparison of the sum of  $\Sigma 3/(\Sigma 9 + \Sigma 27)$  boundaries [50], can also indicate their

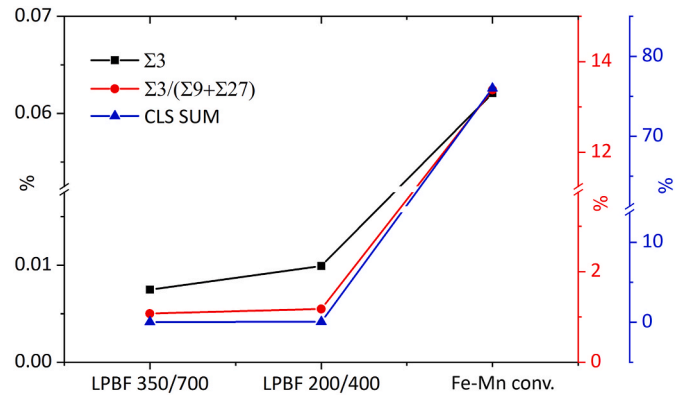


Fig. 6. The frequency of occurrence of certain types of  $\Sigma$  grain boundaries.

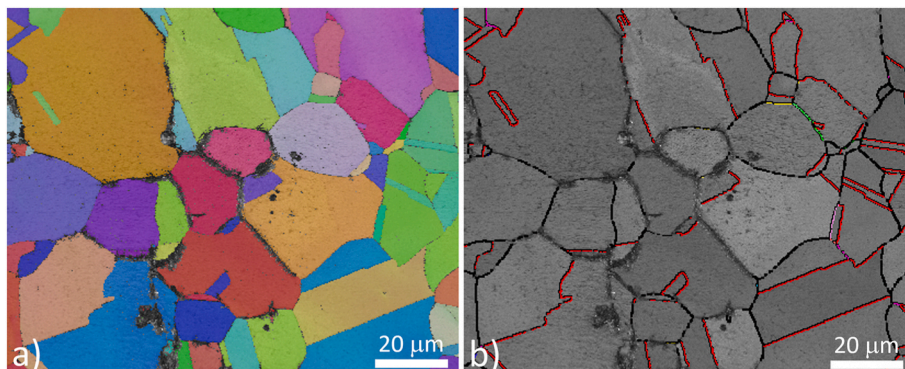


Fig. 5. (a) EBSD IPF Z overlapped with band contrast image, (b) band contrast image with red marked CLS grain boundaries.

corrosion properties. Fig. 6 shows the proportions of  $\Sigma 3$ ,  $\Sigma 3/(\Sigma 9 + \Sigma 27)$  and the sum of all  $\Sigma$  (CLS) boundaries for the LPBF samples (350/700 and 200/400) and conventionally produced sample. The  $\Sigma 3$  boundaries correlate well with the corrosion rate (Fig. 4), where more  $\Sigma 3$  boundaries result in a lower corrosion rate. Ratio  $\Sigma 3/(\Sigma 9 + \Sigma 27)$  boundaries and the sum of all CLS boundaries are in good correlation with the corrosion rate of LPBF samples and conventionally produced ones. However, the main driving force for the corrosion seems to be  $\Sigma 3$  boundaries. The LPBF samples have significantly fewer  $\Sigma 3$  boundaries than conventionally produced samples, which have around six times higher numbers and correlate well with the corrosion rate.

Further, to establish a possible correlation between grain boundaries and corrosion behaviour the EBSD measurements of high-angle grain boundaries (HAGBs) and low-angle grain boundaries (LAGBs) were performed (Fig. 7).

Fig. 7 shows typical EBSD measurements of the LAGBs ( $1^\circ$ – $5^\circ$  and  $5^\circ$ – $15^\circ$ ) and HAGBs ( $15^\circ$ – $180^\circ$ ) boundaries on three different samples. The results of the boundaries' length were calculated from six fields of view. The length of the boundaries is expressed relative to the shortest boundary being 100 %. The length of the HAGBs is very similar for all three samples and differs not more than 20 % in length. Therefore, it can be assumed that the HAGBs are not the key factor influencing the corrosion resistance of those samples. The shortest length of LAGBs ( $5^\circ$ – $15^\circ$ ) is calculated for cast and forged samples, while LPBF processed samples 200/400 and 350/700 have 51 % and 135 % longer boundaries, respectively. The LPBF samples have nearly the same length of LAGBs ( $1^\circ$ – $5^\circ$ ), while on the other hand, cast and forged samples have almost 500 % more of this type of grain boundaries. The reason for the abundance of LAGBs is due to incomplete recrystallization of the material. Because the degradation rate is much higher for LPBF materials, we can conclude that LAGBs have no impact on the corrosion rate. On the other hand, LAGBs can enhance intergranular corrosion in the case of stainless steels where depletion of Cr presents weak points [52]. On the other hand, it is well known that additive manufacturing is susceptible to the formation of porosities during building while conventionally produced material [53] has no porosity. The porosity is, therefore, one of the

parameters which also plays an important role in the corrosion behaviour as the pores in the material represent a weak point enabling the initial intergranular corrosion. The LPBF process parameters influence the formation of porosity so that the same material manufactured by different process parameters can exhibit different amounts of porosity, leading to significant differences in corrosion rates.

Another issue influencing the corrosion behaviour of the LPBF-produced material that should be taken into account is the oxide nanoparticles. Each powder particle is overlaid with a very thin oxide layer (nano to micro size). Some powder particles used in this study contain a micro-oxide layer (Fig. 1(e)). Most of the materials processed by LPBF therefore contain nano-size oxide particles [12], originating from powder particles, which can also increase the corrosion rate. To evaluate the contribution of the oxide nanoparticles in the microstructure to the corrosion rate, we measured nanooxide particles in the matrix (Fig. 8). The measurements were performed on electron channelling contrast images (ECCI) on 20 fields of view with a surface of  $0.9 \mu\text{m}^2$  per field. LPBF 350/700 process parameters generate slightly larger numbers and diameters of oxide particles, which might additionally contribute to the corrosion process.

Based on the results of materials characterisation, it is clear that multiple factors need to be considered when addressing corrosion behaviour. Among previously described ones, there are also some others. One is the grain size; generally, smaller grains mean lower corrosion resistance. The investigated samples contain grains of similar sizes; therefore, this can be excluded as a reason for different corrosion rates. The literature does not report that the presence of dendrite substructure in LPBF samples affects the corrosion rate. It is well known that some steels can be produced without non-metallic inclusions (MnS) [54] and, therefore, exhibit better corrosion resistance than conventionally produced ones. One of the specifics of the LPBF processes is stress accumulation due to rapid solidification, also depending on process parameters (Fig. 3(b) and (d)), which can have an impact on corrosion. The conventionally produced sample in the present work has also accumulated stress (Fig. 3(f)), most probably due to an incomplete normalisation process. While the corrosion rate in this sample is very

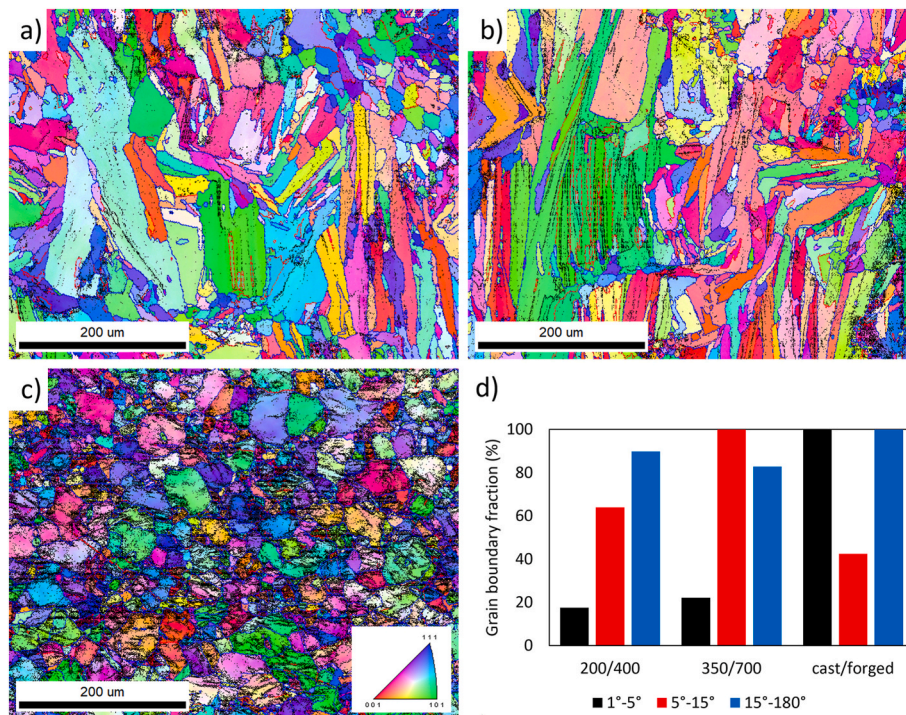
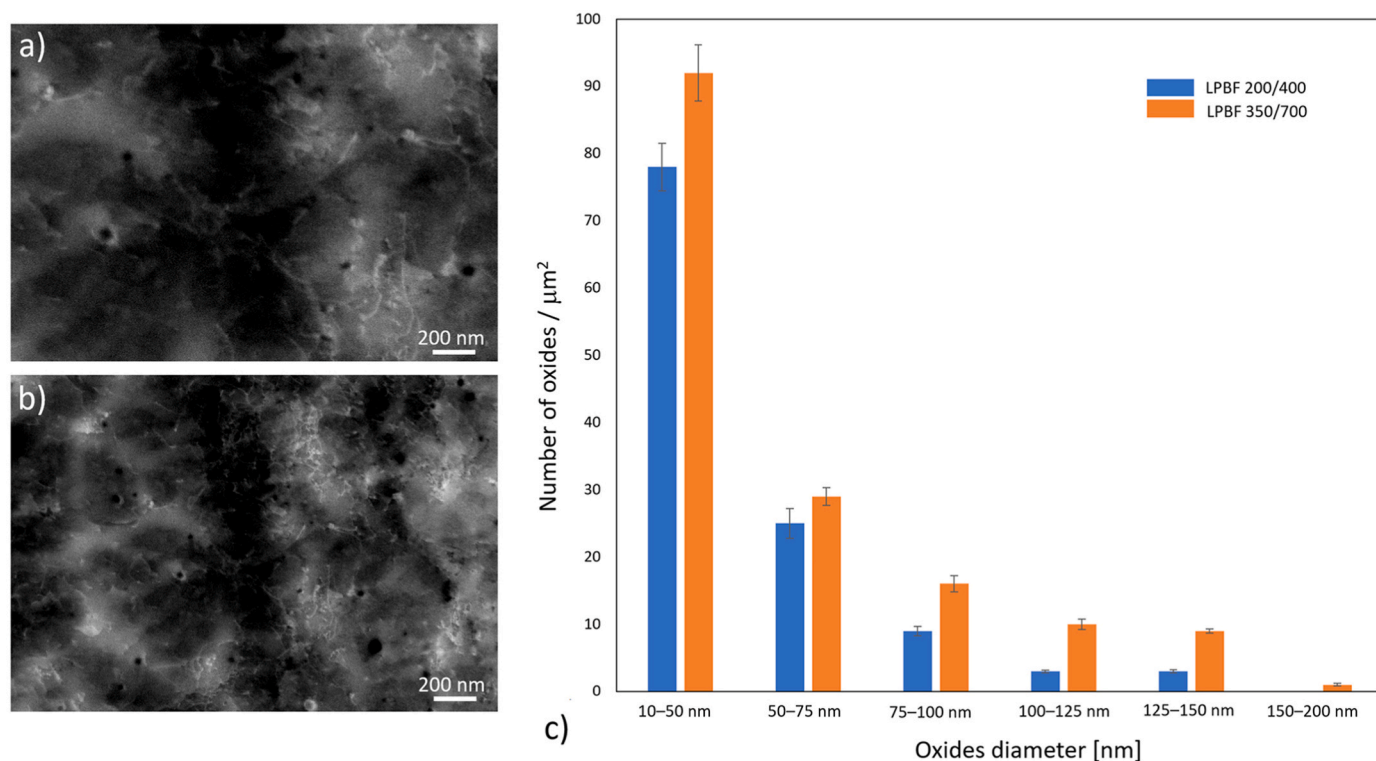


Fig. 7. EBSD IPF-Z grain boundary maps showing HAGBs ( $15^\circ$ – $180^\circ$ ) in blue and LAGBs ( $1^\circ$ – $5^\circ$  and  $5^\circ$ – $15^\circ$ ) in black and red, respectively in (a) LPBF processed Fe-Mn using 200/400 parameters, (b) LPBF processed Fe-Mn using 350/700 parameters and (c) cast and forged Fe-Mn, (d) histogram of grain boundary fraction.



**Fig. 8.** Measurements of oxide particles based on ECCI images of LPBF processed Fe-Mn: (a) 200/400 and (b) 350/700 process parameters, (c) number of oxides per  $\mu\text{m}^2$  in dependence of LPBF process parameters.

low, internal stress is likely not a key factor for corrosion behaviour. The correlation between  $\Sigma$  boundaries and corrosion rate indicates a strong relationship. In general, it can be concluded that the corrosion rate can be driven by the presence of nano oxides and the amount and relation of  $\Sigma$  boundaries.

XPS measurements were used to observe the initial oxidation process of the Fe-Mn alloy to evaluate the oxide film of Fe and Mn oxides. Understanding the initial oxidation process of Fe-Mn alloy is crucial as it creates a surface for biofilm-forming cells and organisms to attach to [55].

Detailed high-resolution XPS spectra in Fig. 9 show scans of metallic and oxide components of both Fe  $2p_{3/2}$  and Mn  $2p_{3/2}$  transitions. Four peaks were utilised to fit the Fe  $2p_{3/2}$  (Fig. 9(a)), including metallic and three oxide peaks:  $\text{Fe}_2\text{O}_3$ ,  $\text{Fe}_3\text{O}_4$ , and FeO. The component binding energy differences were fixed at values from the literature [56], and the full width at half maximum (FWHM) for the three oxide peaks were fixed to be the same, while the metallic peak was narrower. To analyse the Mn  $2p_{3/2}$ , four peaks were fitted similarly and corresponded directly as described in [57]. The Mn  $2p_{3/2}$  transitions for the sample were shown in Fig. 9(b) after different sputtering times. As discussed previously, only a  $2p_{3/2}$  peak for Fe and Mn was fitted at each depth. The  $\text{Ar}^+$  ion sputtering can change the oxidation state due to ion-sputtering-induced effects of metallic species, and the results may not be entirely accurate [58], but comparing oxidation levels is possible. The areas of the three oxide peak components were added to approximate the total Fe and Mn oxides. The oxide components decreased in intensity with sputtering until only the metallic components of Fe and Mn were left.

The XPS depth profiles (Fig. 9(c) and (d)) illustrate the formation of an oxide film consisting of Fe and Mn oxides at the surface and in the initial inner region, and predominantly Mn oxide in the inner region, along with pure metals. At the same time, there are negligible amounts of unoxidized Mn or Fe in the top oxide layer. The proportion of unoxidized metals in the upper layer of the oxide coating is significantly lower than that of the oxidized metals. This composition of the initial

oxide film with metallic Fe and Mn components is divided in the scheme in Fig. 9(c). To estimate the actual depth in XPS depth profiles, we utilized a correlation based on the  $\text{SiO}_2$  sputter rate of our equipment with the correction from the as proposed Baer et al. [59] the sputtering rates of other oxide films relative to the sputtering rate of  $\text{SiO}_2$ .

These results indicate that the electrochemical stability of the alloy decreased significantly after LPBF processing. It should be noted that the standard reduction potential of pure Mn is lower than that of Fe, at  $-1.18$  V compared to  $-0.44$  V, respectively [2]. Consequently, when Fe is alloyed with Mn, the corrosion resistance decreases, and unstable Mn oxides form on the surface in combination with Fe oxide, which possesses a lower passivity coefficient than pure Fe oxide (Fig. 9(c) and (d)). As a result, the surface passivity significantly decreased, leading to accelerated electrochemical corrosion when pitting corrosion occurred. This observation may explain the enhanced corrosion current observed during the electrochemical tests of LPBF-produced Fe-Mn alloy.

### 3.2. Biocompatibility

*In vitro* tests were conducted using MG-63 human osteoblast-like osteosarcoma cells to examine the biocompatibility of the studied Fe-Mn alloys.

Using differential staining and fluorescence microscopy, the cell adhesion density and viability of cells grown on control glass surface, cast and forged sample, LPBF (200/400) sample and LPBF (350/700) sample were quantified (Fig. 10). Density of attached viable cells was  $125 \pm 27$  cells/ $\text{mm}^2$  for control glass surface,  $112 \pm 26$  cells/ $\text{mm}^2$  for cast/forged sample,  $107 \pm 40$  cells/ $\text{mm}^2$  for LPBF (200/400) sample, and  $90 \pm 30$  cells/ $\text{mm}^2$  for LPBF (350/700) sample. In all analysed samples, the percentage of dead cells was lower than 10 %. The lowest viability of adhered MG-63 cells was on LPBF 200/400 samples (9.1 % of dead cells), and the highest was on control glass coverslips (3.8 % of dead cells).

Differences in the morphology of the MG-63 cells attached to

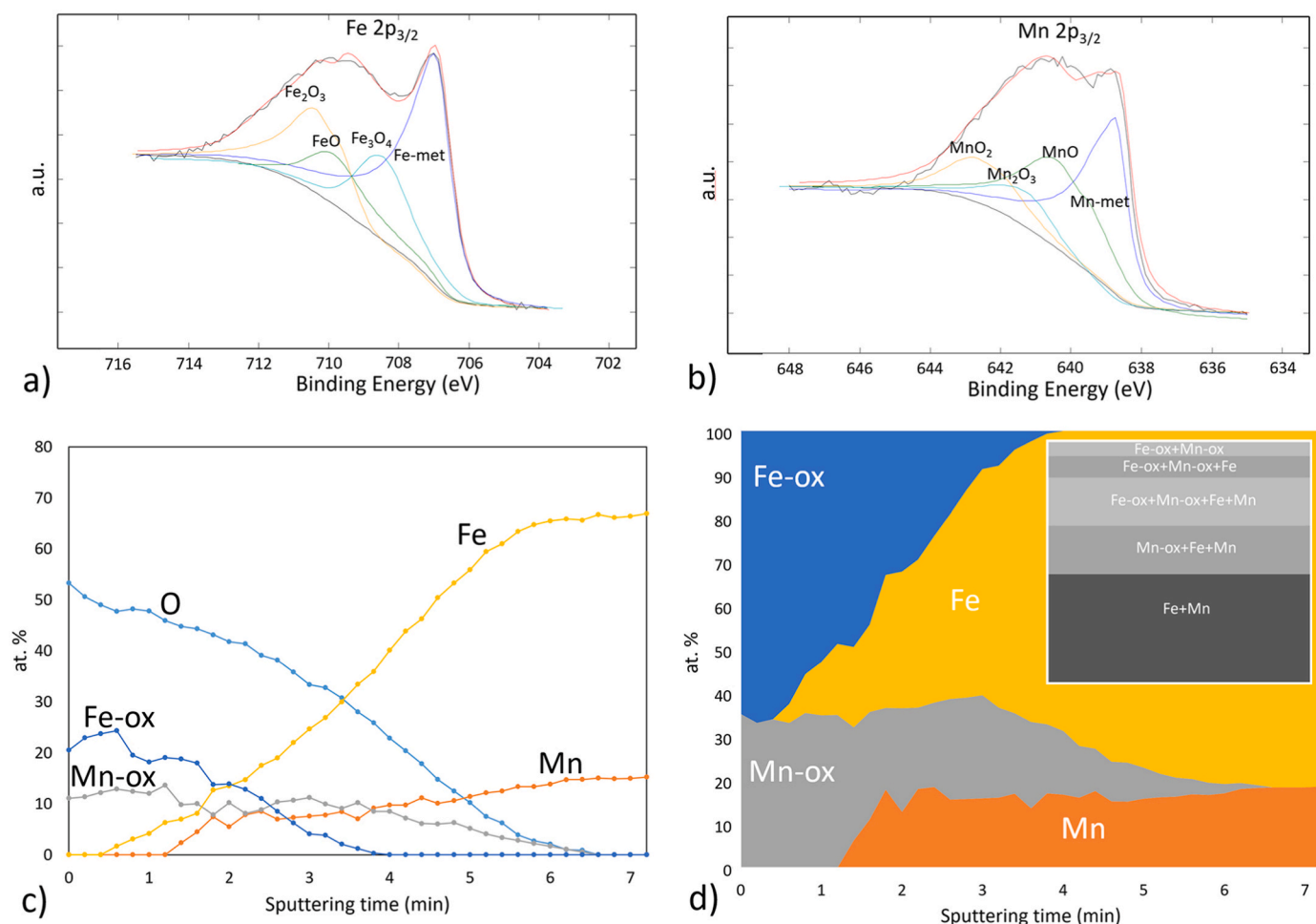


**Fig. 9.** XPS analysis of LPBF 350/700 in the initial condition. Examples of: (a) fitted Fe 2p<sub>3/2</sub>, and (b) Mn 2p<sub>3/2</sub> XPS spectra. (c) XPS depth profiles of all elements and (d) XPS depth profile of just metallic ions, without oxygen. The inset is a visual representation of how the oxide/metallic layers initially oxidize, along with their calculated thickness based on these depth profiles.

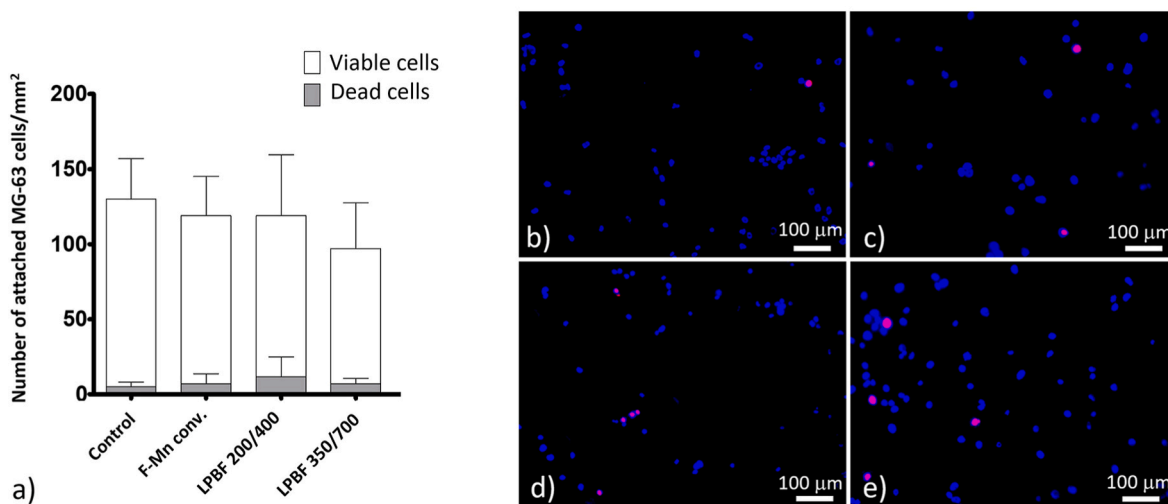


**Fig. 10.** Adhesion of MG-63 cells to different surfaces after 24-hour incubation: (a) cell density and viability of MG-63 cells adhered to the control glass surface, cast and forged sample, LPBF (200/400) sample and LPBF (350/700) sample; (b-e) representative fluorescence microscopy images of MG-63 cells adhered to (b) control glass surface, (c) cast and forged sample, (d) LPBF (200/400) sample and (e) LPBF (350/700) sample. The nuclei of viable cells are stained blue with Hoechst 33342, while nuclei of dead cells (cells with damaged plasmalemma) are stained red with Propidium iodide.

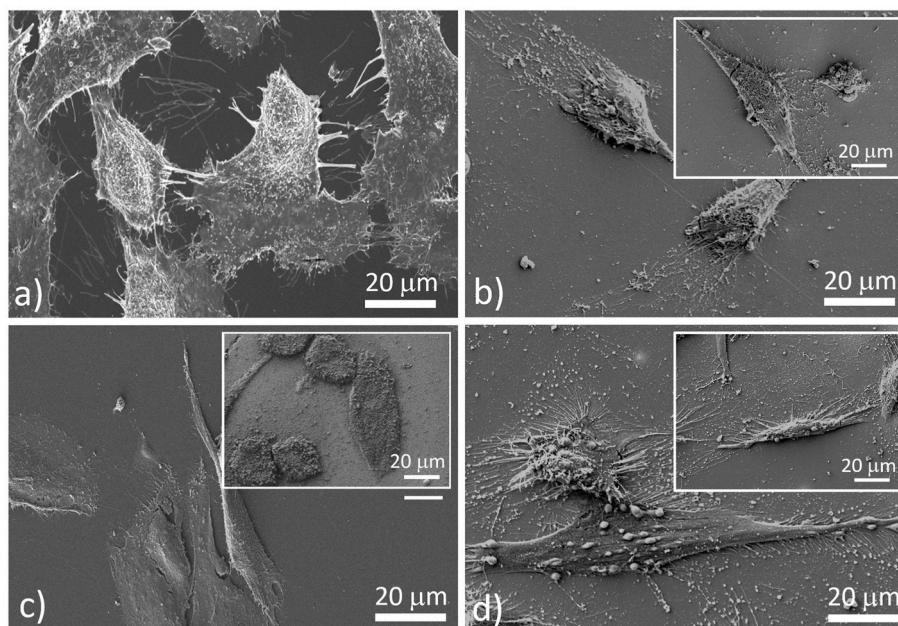


**Fig. 11.** SEM images of MG-63 cells on a: (a) control glass surface, (b) cast and forged, (c) LPBF (200/400) and (d) LPBF (350/700) sample.

different materials were examined using SEM. From the tested samples, the representative images of cell morphology were selected, as shown in Fig. 11. In the control glass sample (Fig. 11(a)), the majority of cells were spread through the surface, with visible lamellipodia and filopodia. Similar cell morphology was also observed in the cast and forged samples (Fig. 11(b)) and on the LPBF (350/700) samples (Fig. 11(d)). However, the cells were slightly less flattened here, whereas, in the LPBF (200/400) samples (Fig. 11 (c)), the cells had similar morphology as on glass samples. Still, in some areas, cells were smaller in diameter, thicker, and had less visible lamellipodia and filopodia (inset of Fig. 11 (c)).

The interactions between cells and materials depend largely on the surface properties of the material, which determine the adsorption pattern of the adsorbed molecules and, thus, the behaviour of the cells upon contact [37]. The results showed no significant difference in the density of attached cells (viable and dead) between the different Fe-Mn materials compared to a nontoxic control glass coverslip, indicating that all tested materials allow good cell adhesion and are not cytotoxic, at least in the short term. SEM examination of the cells on the different samples showed that the cells on the LPBF (350/700) samples had a similar flattened morphology with visible lamellipodia and filopodia as the cells on the control coverslips. In contrast, cells on LPBF (200/400) samples were smaller in diameter, thicker, and had less visible lamellipodia and filopodia. It is known that adherent cells require a suitable surface to which they can adhere and proliferate. The cells actively probe the physicochemical properties of their environment and form protrusions called lamellipodia - structures important for cell spreading and polarisation - as well as hair-like structures called filopodia, which gather spatial, topographical and chemical information from their surroundings [60,61]. It might be speculated that the changed morphology of the cells on LPBF (200/400) may indicate that the cells, although they adhered to a similar extent as the cells on the coverslips, would not spread and proliferate to the same extent as the control cells in the longer duration experiments. The tested materials did not significantly differ in biocompatibility; however, LPBF (200/400) material appears to be slightly less favourable for cell spreading and proliferation as tested in a 24-hour setting.

#### 4. Conclusions

The present study investigated the Fe-Mn alloys produced by the LPBF process using alloy powder to evaluate their bioresorbable properties and their relation to the microstructure. The investigation was also carried out on conventionally produced (cast/forged) Fe-Mn alloy for comparison. The following conclusions can be drawn:

- Specific chemical composition (1.2 wt.% C and 32 wt.% Mn), regardless of processing routes (LPBF or conventionally produced), leads to the formation of austenitic microstructure, which is known for its antiferromagnetic behaviour required for MRI compatibility.
- By changing laser power and scan speed, although keeping the input energy the same, different microstructure, grain boundaries, and misorientation intensities were observed.
- The lowest corrosion rate was observed in conventionally produced alloy, followed by LPBF 200/400 and LPBF 350/700. One of the main reasons for differences in corrosion rate can be attributed to grain boundary types. A higher proportion of CLS boundaries makes the material more corrosion-resistant. The grain boundary type affects the corrosion rate, whereas the  $\Sigma 3$  boundaries contribute significantly to the lower corrosion rate.
- The initial oxidation process observed by XPS reveals Fe- and Mn-oxides on the surface in the proportion of 2/3 to 1/3, respectively. The amount of Fe-oxides decreases faster by depth compared to Mn-oxides and, therefore, affects the creation of a surface for biofilm-forming cells and organisms to attach to.
- Biocompatibility tests have shown that various Fe-Mn materials are not cytotoxic and allow good cell adhesion. The results suggest that cell spreading and proliferation may be slightly less favourable on the LPBF (200/400) material.

A comprehensive microstructure investigation supported by *in vitro* biocompatibility tests and cell analysis showed that Fe-Mn produced by the LPBF process can be suitable for different implant applications.

#### Data availability

Data is available in the open repository DiRRROS with PID <http://hdl.handle.net/20.500.12556/DiRRROS-18671>.

## Credit author statement

**Matjaž Godec:** Conceptualization, Funding acquisition, Writing – original draft, Writing – review & editing, Supervision. **Jakob Kraner:** Investigation, Data curation, Writing – original draft. **Danijela Skobir Balantič:** Investigation, Writing – original draft, Writing – review & editing. **Irena Paulin:** Investigation, Writing – review & editing. **Damjana Drobne:** Investigation, Writing – original draft, Writing – review & editing. **Veno Kononenko:** Investigation, Writing – original draft, Writing – review & editing. **Aleksandra Kocijan:** Investigation, Writing – original draft, Writing – review & editing. **Paul McGuinness:** Writing – review & editing. **Črtomir Donik:** Investigation, Methodology, Data curation, Writing – review & editing.

## Declaration of Competing Interest

The authors declare that they have no known competing financial interests or personal relationships that could have appeared to influence the work reported in this paper.

## Acknowledgements

This work was financially supported by the Slovenian Research and Innovation Agency (core fundings No. P2-0132, P1-0207, Infrastructure IO-0006 and Project No. J2-1729).

## References

- Li C, Guo C, Fitzpatrick V, Ibrahim A, Zwierstra MJ, Hanna P, Lechtig A, Nazarian A, Lin SJ, Kaplan DL. Design of biodegradable, implantable devices towards clinical translation. *Nat. Rev. Mater.* 2020;5:61–81. <https://doi.org/10.1038/s41578-019-0150-z>.
- Venezuela J, Dargusch MS. Addressing the slow corrosion rate of biodegradable Fe-Mn: Current approaches and future trends. *Curr. Opin. Solid State Mater. Sci.* 2020;24:100822. <https://doi.org/10.1016/j.cossms.2020.100822>.
- Khan AR, Grewal NS, Zhou C, Yuan K, Zhang H-J, Jun Z. Recent advances in biodegradable metals for implant applications: Exploring in vivo and in vitro responses. *Results Eng* 2023;20:101526. <https://doi.org/10.1016/j.rineng.2023.101526>.
- Kraus T, Moszner F, Fischerauer S, Fiedler M, Martinelli E, Eichler J, Witte F, Willbold E, Schinhammer M, Meischel M, Uggowitz P, Löffler JF, Weinberg A. Biodegradable Fe-based alloys for use in osteosynthesis: Outcome of an in vivo study after 52weeks. *Acta Biomater* 2014;10:3346–53. <https://doi.org/10.1016/j.actbio.2014.04.007>.
- Čapek J, Stehlíková K, Michalčová A, Msallamová Š, Vojtěch D. Microstructure, mechanical and corrosion properties of biodegradable powder metallurgical Fe-2 wt% X (X = Pd, Ag and C) alloys. *Mater. Chem. Phys.* 2016;181:501–11. <https://doi.org/10.1016/j.matchemphys.2016.06.087>.
- Kwon H, Park K. Effects of Manganese on the Passivity of Fe-18Cr- $x$ C/ $x$ Mn ( $x = 0, 6, 12$ ). *ECS Trans.* 2006;1:313. <https://doi.org/10.1149/1.2215515>.
- Bastidas DM, Röss J, Bosch J, Martin U. Corrosion Mechanisms of High-Mn Twinning-Induced Plasticity (TWIP) Steels: A Critical Review. *Metals (Basel)*. 2021; 11. <https://doi.org/10.3390/met11020287>.
- Hermawan H, Moravej M, Dubé D, Fiset M, Mantovani D. Degradation Behaviour of Metallic Biomaterials for Degradable Stents. *Adv. Mater. Res.* 2007;15–17: 113–8. <https://doi.org/10.4028/www.scientific.net/AMR.15-17.113>.
- Hermawan H, Purnama A, Dube D, Couet J, Mantovani D. Fe-Mn alloys for metallic biodegradable stents: Degradation and cell viability studies. *Acta Biomater* 2010;6:1852–60. <https://doi.org/10.1016/j.actbio.2009.11.025>.
- Hermawan H, Dubé D, Mantovani D. Degradable metallic biomaterials: Design and development of Fe-Mn alloys for stents. *J. Biomed. Mater. Res. Part A.* 2009;9999A. <https://doi.org/10.1002/jbm.a.32224>. NA-NA.
- Lee Y-K, Jun J-H, Choi C-S. Damping Capacity in Fe-Mn Binary Alloys. *ISIJ Int.* 1997;37:1023–30. <https://doi.org/10.2355/isijinternational.37.1023>.
- Donik Č, Kraner J, Kocijan A, Paulin I, Godec M. Evolution of the  $\epsilon$  and  $\gamma$  phases in biodegradable Fe-Mn alloys produced using laser powder-bed fusion. *Sci. Rep.* 2021;11:19506. <https://doi.org/10.1038/s41598-021-99042-0>.
- Hermawan H, Alamdari H, Mantovani D, Dubé D. Iron-manganese: new class of metallic degradable biomaterials prepared by powder metallurgy. *Powder Metall* 2008;51:38–45. <https://doi.org/10.1179/174329008X284868>.
- Schinhammer M, Gerber I, Hänzl AC, Uggowitz P. On the cytocompatibility of biodegradable Fe-based alloys. *Mater. Sci. Eng. C.* 2013;33:782–9. <https://doi.org/10.1016/j.msec.2012.11.002>.
- Hufenbach J, Wendrock H, Kochta F, Kühn U, Gebert A. Novel biodegradable Fe-Mn-C-S alloy with superior mechanical and corrosion properties. *Mater. Lett.* 2017; 186:330–3. <https://doi.org/10.1016/j.matlet.2016.10.037>.
- Yeganeh M, Eskandari M, Alavi-Zaree SR. A Comparison Between Corrosion Behaviors of Fine-Grained and Coarse-Grained Structures of High-Mn Steel in NaCl Solution. *J. Mater. Eng. Perform.* 2017;26:2484–90. <https://doi.org/10.1007/s11665-017-2685-8>.
- Eskandari MYJASM, Mohtadi-Bonab MA, Odeshi AG. High-strain-rate deformation behaviour of new high-Mn austenitic steel during impact shock-loading. *Mater. Sci. Technol.* 2019;35:77–88. <https://doi.org/10.1080/02670836.2018.1540507>.
- Hufenbach J, Kochta F, Wendrock H, Voß A, Giebeler L, Oswald S, Pilz S, Kühn U, Lode A, Gelinsky M, Gebert A. S and B microalloying of biodegradable Fe-30Mn-1C - Effects on microstructure, tensile properties, in vitro degradation and cytotoxicity. *Mater. Des.* 2018;142:22–35. <https://doi.org/10.1016/j.matdes.2018.01.005>.
- Mandal S, Kishore V, Bose M, Nandi SK, Roy M. In vitro and in vivo degradability, biocompatibility and antimicrobial characteristics of Cu added iron-manganese alloy. *J. Mater. Sci. Technol.* 2021;84:159–72. <https://doi.org/10.1016/j.jmst.2020.12.029>.
- Hong D, Chou D-T, Velikokhatnyi OI, Roy A, Lee B, Swink I, Issaev I, Kuhn HA, Kumta PN. Binder-jetting 3D printing and alloy development of new biodegradable Fe-Mn-Ca/Mg alloys. *Acta Biomater* 2016;45:375–86. <https://doi.org/10.1016/j.actbio.2016.08.032>.
- Sotoudehbagha P, Sheibani S, Khakbiz M, Ebrahimi-Barough S, Hermawan H. Novel antibacterial biodegradable Fe-Mn-Ag alloys produced by mechanical alloying. *Mater. Sci. Eng. C.* 2018;88:88–94. <https://doi.org/10.1016/j.msec.2018.03.005>.
- Dargusch MS, Venezuela J, Dehghan-Manshadi A, Johnston S, Yang N, Mardon K, Lau C, Allavena R. In Vivo Evaluation of Bioabsorbable Fe-35Mn-1Ag: First Reports on In Vivo Hydrogen Gas Evolution in Fe-Based Implants. *Adv. Healthc. Mater.* 2021;10:2000667. <https://doi.org/10.1002/adhm.202000667>.
- Saliba L, Sammut K, Tonna C, Pavli F, Valdramidis V, Gatt R, Giordmaina R, Camilleri L, Atanasio W, Buhagiar J, Schembri Wismayer P. FeMn and FeMnAg biodegradable alloys: An in vitro and in vivo investigation. *Heliyon* 2023;9: e15671. <https://doi.org/10.1016/j.heliyon.2023.e15671>.
- Liu R-Y, He R-G, Xu L-Q, Guo S-F. Design of Fe-Mn-Al Alloys as Potential Candidates for Biodegradable Metals. *Acta Metall. Sin. (English Lett.)* 2018;31: 584–90. <https://doi.org/10.1007/s40195-018-0702-z>.
- Wang C, Tonna C, Mei D, Buhagiar J, Zheludkevich ML, V Lamaka S. Biodegradation behaviour of Fe-based alloys in Hanks' Balanced Salt Solutions: Part II. The evolution of local pH and dissolved oxygen concentration at metal interface. *Bioact. Mater.* 2022;7:412–25. <https://doi.org/10.1016/j.bioactmat.2021.05.014>.
- Gambaro S, Paternoster C, Occhionero B, Fiocchi J, Biffi CA, Tuissi A, Mantovani D. Mechanical and degradation behavior of three Fe-Mn-C alloys for potential biomedical applications. *Mater. Today Commun.* 2021;27:102250. <https://doi.org/10.1016/j.mtcomm.2021.102250>.
- Liu P, Zhang D, Dai Y, Lin J, Li Y, Wen C. Microstructure, mechanical properties, degradation behavior, and biocompatibility of porous Fe-Mn alloys fabricated by sponge impregnation and sintering techniques. *Acta Biomater* 2020;114:485–96. <https://doi.org/10.1016/j.actbio.2020.07.048>.
- Paul B, Hofmann A, Weinert S, Frank F, Wolff U, Krautz M, Edelmann J, Gee MW, Reeps C, Hufenbach J. Effect of Blasting Treatments on the Surface Topography and Cell Adhesion on Biodegradable FeMn-Based Stents Processed by Laser Powder Bed Fusion. *Adv. Eng. Mater.* 2022;24:2200961. <https://doi.org/10.1002/adem.202200961>.
- Carluccio D, Xu C, Venezuela J, Cao Y, Kent D, Birmingham M, Demir AG, Previtali B, Ye Q, Dargusch M. Additively manufactured iron-manganese for biodegradable porous load-bearing bone scaffold applications. *Acta Biomater* 2020;103:346–60. <https://doi.org/10.1016/j.actbio.2019.12.018>.
- Liu P, Wu H, Liang L, Song D, Liu J, Ma X, Li K, Fang Q, Tian Y, Baker I. Microstructure, mechanical properties and corrosion behavior of additively-manufactured Fe-Mn alloys. *Mater. Sci. Eng. A.* 2022;852:143585. <https://doi.org/10.1016/j.msea.2022.143585>.
- Nie Y, Chen G, Peng H, Tang S, Zhou Z, Pei F, Shen B. In vitro and 48 weeks in vivo performances of 3D printed porous Fe-30Mn biodegradable scaffolds. *Acta Biomater* 2021;121:724–40. <https://doi.org/10.1016/j.actbio.2020.12.028>.
- Carluccio D, Demir AG, Birmingham MJ, Dargusch MS. Challenges and Opportunities in the Selective Laser Melting of Biodegradable Metals for Load-Bearing Bone Scaffold Applications. *Metall. Mater. Trans. A.* 2020;51:3311–34. <https://doi.org/10.1007/s11661-020-05796-z>.
- Carluccio D, Demir AG, Caprio L, Previtali B, Birmingham MJ, Dargusch MS. The influence of laser processing parameters on the densification and surface morphology of pure Fe and Fe-35Mn scaffolds produced by selective laser melting. *J. Manuf. Process.* 2019;40:113–21. <https://doi.org/10.1016/j.jmapro.2019.03.018>.
- Dargusch MS, Dehghan-Manshadi A, Shahbazi M, Venezuela J, Tran X, Song J, Liu N, Xu C, Ye Q, Wen C. Exploring the Role of Manganese on the Microstructure, Mechanical Properties, Biodegradability, and Biocompatibility of Porous Iron-Based Scaffolds. *ACS Biomater. Sci. Eng.* 2019;5:1686–702. <https://doi.org/10.1021/acsbmaterials.8b01497>.
- Salama M, Vaz MF, Colaço R, Santos C, Carmezim M. Biodegradable Iron and Porous Iron: Mechanical Properties, Degradation Behaviour, Manufacturing Routes and Biomedical Applications. *J. Funct. Biomater.* 2022;13. <https://doi.org/10.3390/jfb13020072>.
- Bernard M, Jubeli E, Pungente MD, Yagoubi N. Biocompatibility of polymer-based biomaterials and medical devices – regulations, in vitro screening and risk-management. *Biomater. Sci.* 2018;6:2025–53. <https://doi.org/10.1039/C8BM00518D>.

- [37] Anselme K. Osteoblast adhesion on biomaterials. *Biomaterials* 2000;21:667–81. [https://doi.org/10.1016/S0142-9612\(99\)00242-2](https://doi.org/10.1016/S0142-9612(99)00242-2).
- [38] Hočevar M, Setina Batič B, Godec M, Kononenko V, Drobne D, Gregorčič P. The interaction between the osteosarcoma cell and stainless steel surface, modified by high-fluence, nanosecond laser pulses. *Surf. Coatings Technol.* 2020;394:125878. <https://doi.org/10.1016/j.surfcoat.2020.125878>.
- [39] Sun Y, Chen L, Liu N, Wang H, Liang C. Laser-modified Fe–30Mn surfaces with promoted biodegradability and biocompatibility toward biological applications. *J. Mater. Sci.* 2021;56:13772–84. <https://doi.org/10.1007/s10853-021-06139-y>.
- [40] Gorejová R, Haverová L, Oriňaková R, Oriňak A, Oriňak M. Recent advancements in Fe-based biodegradable materials for bone repair. *J. Mater. Sci.* 2019;54:1913–47. <https://doi.org/10.1007/s10853-018-3011-z>.
- [41] ISO 10271:2020; Dentistry-Corrosion Test Methods for Metallic Materials. ISO/TC 106/SC2 Prosthodontic Materials 2020. ISO Copyright Office: Geneva, Switzerland, 2020, (n.d.).
- [42] ISO 22674:2022; Dentistry—Metallic Materials for Fixed and Removable Restorations and Appliances. International Organization for Standardization: Geneva, Switzerland, 2022., (n.d.).
- [43] Mede T, Kocjan A, Paulin I, Godec M. Laser powder-bed fusion of biodegradable Fe–Mn alloy: melt-pool solidification. *Appl. Phys. A.* 2022;128:739. <https://doi.org/10.1007/s00339-022-05851-z>.
- [44] Shen Y, Yang S, Liu J, Liu H, Zhang R, Xu H, He Y. Study on Micro Segregation of High Alloy Fe–Mn–C–Al Steel. *Steel Res. Int.* 2019;90:1800546. <https://doi.org/10.1002/srin.201800546>.
- [45] Kraner J, Medved J, Godec M, Paulin I. Thermodynamic Behavior of Fe–Mn and Fe–Mn–Ag Powder Mixtures during Selective Laser Melting. *Metals (Basel)*. 2021;11. <https://doi.org/10.3390/met11020234>.
- [46] Liu P, Li G, Liu B, Liao C, Baker I, Wu H. Tribocorrosion behavior of additively-manufactured Fe–Mn alloys. *Mater. Lett.* 2023;337:133949. <https://doi.org/10.1016/j.matlet.2023.133949>.
- [47] Schinhammer M, Hänzli AC, Löffler JF, Uggowitzer PJ. Design strategy for biodegradable Fe-based alloys for medical applications. *Acta Biomater* 2010;6:1705–13. <https://doi.org/10.1016/j.actbio.2009.07.039>.
- [48] ASTM Standard G102-89(2015)e1 Standard Practice for Calculation of Corrosion Rates and Related Information from Electrochemical Measurements, (n.d.). <https://doi.org/10.1520/G0102-89R15E01>.
- [49] McCafferty E. Validation of corrosion rates measured by the Tafel extrapolation method. *Corros. Sci.* 2005;47:3202–15. <https://doi.org/10.1016/j.corsci.2005.05.046>.
- [50] Zhang C, Lin L, Chen R, Zhang L, Shao Z. Grain Boundary Engineering and Its Effect on Intergranular Corrosion Resistance of a Ni–Cr–Mo Based C276 Superalloy. *Crystals* 2022;12. <https://doi.org/10.3390/cryst12111625>.
- [51] Randle V. Twinning-related grain boundary engineering. *Acta Mater* 2004;52:4067–81. <https://doi.org/10.1016/j.actamat.2004.05.031>.
- [52] Yeganeh M, Rezvani MH, Laribaghaj SM. Electrochemical behavior of additively manufactured 316L stainless steel in H<sub>2</sub>SO<sub>4</sub> solution containing methionine as an amino acid. *Colloids Surfaces A Physicochem. Eng. Asp.* 2021;627:127120. <https://doi.org/10.1016/j.colsurfa.2021.127120>.
- [53] Paulin I. Influence of different treatments on the corrosion behaviour of an Fe-based biodegradable alloy. *Mater. Tehnol.* 2021;55:155–8. <https://doi.org/10.17222/mit.2020.252>.
- [54] Suzuki M, Yamaguchi R, Murakami K, Nakada M. Inclusion Particle Growth during Solidification of Stainless Steel. *Isij Int. - ISIJ INT.* 2001;41:247–56. <https://doi.org/10.2355/isijinternational.41.247>.
- [55] Donik C, Kocjan A, Paulin I, Hočevar M, Gregorčič P, Godec M. Improved biodegradability of Fe–Mn alloy after modification of surface chemistry and topography by a laser ablation. *Appl. Surf. Sci.* 2018;453:383–93. <https://doi.org/10.1016/j.apsusc.2018.05.066>.
- [56] Lynch B, Wiame F, Maurice V, Marcus P. XPS study of oxide nucleation and growth mechanisms on a model FeCrNiMo stainless steel surface. *Appl. Surf. Sci.* 2022;575:151681. <https://doi.org/10.1016/j.apsusc.2021.151681>.
- [57] Ilton ES, Post JE, Heaney PJ, Ling FT, Kerisit SN. XPS determination of Mn oxidation states in Mn (hydr)oxides. *Appl. Surf. Sci.* 2016;366:475–85. <https://doi.org/10.1016/j.apsusc.2015.12.159>.
- [58] Leygraf C, Hultquist G. Initial oxidation stages on Fe Cr(100) and Fe Cr(110) surfaces. *Surf. Sci.* 1976;61:69–84. [https://doi.org/10.1016/0039-6028\(76\)90408-8](https://doi.org/10.1016/0039-6028(76)90408-8).
- [59] Baer DR, Engelhard MH, Lea AS, Nachimuthu P, Droubay TC, Kim J, Lee B, Mathews C, Opila RL, V Saraf L, Stickle WF, Wallace RM, Wright BS. Comparison of the sputter rates of oxide films relative to the sputter rate of SiO<sub>2</sub>. *J. Vac. Sci. Technol. A.* 2010;28:1060–72. <https://doi.org/10.1116/1.3456123>.
- [60] Biggs MJP, Richards RG, Dalby MJ. Nanotopographical modification: a regulator of cellular function through focal adhesions. *Nanomedicine Nanotechnology, Biol. Med.* 2010;6:619–33. <https://doi.org/10.1016/j.nano.2010.01.009>.
- [61] Mogilner A, Rubinstein B. The Physics of Filopodial Protrusion. *Biophys. J.* 2005;89:782–95. <https://doi.org/10.1529/biophysj.104.056515>.